Statistical fluctuations in HfO$_x$ resistive-switching memory (RRAM): Part II - Random telegraph noise

S. Ambrogio, *Student Member, IEEE*, S. Balatti, *Student Member, IEEE*, A. Cubeta, *Student Member, IEEE*,
A. Calderoni, N. Ramaswamy, *Senior Member, IEEE*, D. Ielmini, *Senior Member, IEEE*

Abstract—A key concern for resistive switching memory (RRAM) is the read noise, due to the structural, chemical and electrical modifications taking place at the localized current path, or conductive filament (CF). Read noise typically appears as a random telegraph noise (RTN), where the current randomly fluctuates between ON and OFF levels. This work addresses RTN in RRAM, providing physical interpretations and models for the dependence on the programming and read conditions. First, we explain the RTN dependence on the compliance current during set transition in terms of the size-dependent depletion of carriers within the CF. Then we discuss the bias-dependence of the RTN switching times and amplitude, which can be explained by Joule heating and Poole-Frenkel (PF) barrier modifications arising from the electrostatics of the RTN fluctuating center.

Keywords: resistive switching memory (RRAM), noise fluctuations, random telegraph noise.

I. INTRODUCTION

Defect-based switching and conduction in resistive switching memory (RRAM) causes stochastic effects during both programming and read. The individual migration events during set and reset results in cycle-to-cycle variations of the resistance in the set and reset states, as discussed in the companion paper [1]. While set/reset variability might be controlled by proper program/verify procedures, read current fluctuations due to low-frequency noise can hardly be avoided [2]–[10]. For fast read and reliable operation of RRAM, the read noise dependence on time, programming conditions and read voltage must be carefully studied.

This work addresses random telegraph noise (RTN) in RRAM, namely a random two-level fluctuation of read current during time. We show that RTN can be understood by the charging of a trap at or close to the surface of the CF, which results in a local time-dependent depletion of the carriers within the CF. A numerical model is developed, accounting for the dependence of RTN amplitude on I_C as a result of the different impact of depletion on the CF current. The model also accounts for 4-level complex RTN in RRAM, which is attributed to the independent fluctuation of two traps. Finally, we discuss the bias dependence of RTN switching times and amplitude. The switching times are shown to decrease with
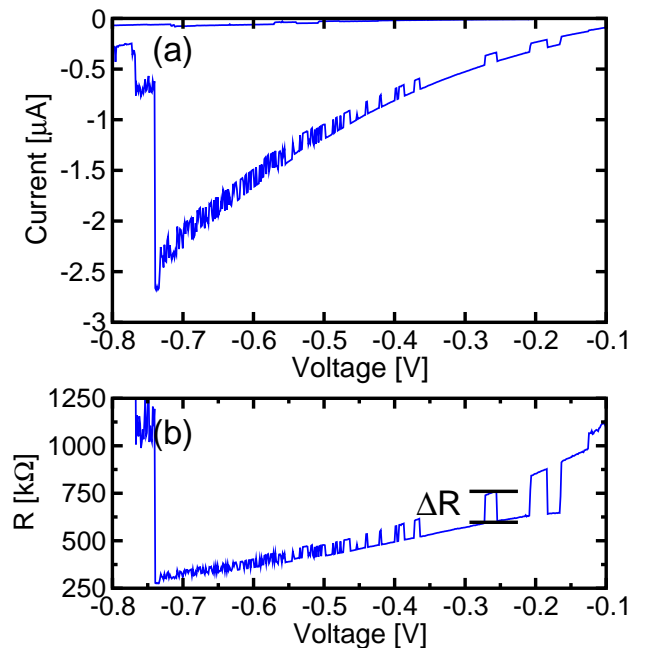
Fig. 1. Measured *I-V* curve for negative voltage with relatively large RTN (a) and the corresponding R as a function of voltage (b). The RRAM device was preliminary programmed in the set state at $I_C = 5$ μA.

the read voltage, which is attributed to the local Joule heating in the CF accelerating the switching kinetics of the RTN trap. The relative change of resistance during RTN is shown to depend differently on bias for low and high resistance CFs, which is explained in terms of the different transport regimes in the CF, namely metallic conduction or Poole-Frenkel (PF) hopping transport. A preliminary study on RTN modeling was previously reported in [10]. In this work, we extend the analysis of [10] by reporting complex RTN due to multiple traps, the temperature-dependence of RTN and time-dependent simulations for variable programming and reading conditions.

II. RANDOM TELEGRAPH NOISE (RTN)

Fig. 1a shows the measured current-voltage (*I-V*) characteristics at negative voltage for a RRAM device with HfO$_x$ switching layer in one-transistor/one-resistor (1T1R) configuration. Details of the device structure and of the integrated select transistor can be found in [1]. A compliance current $I_C = 5$ μA was used during set operation at positive voltage by operating the select transistor at a gate voltage $V_G = 0.7$ V. The measured current displays typical RTN at both positive
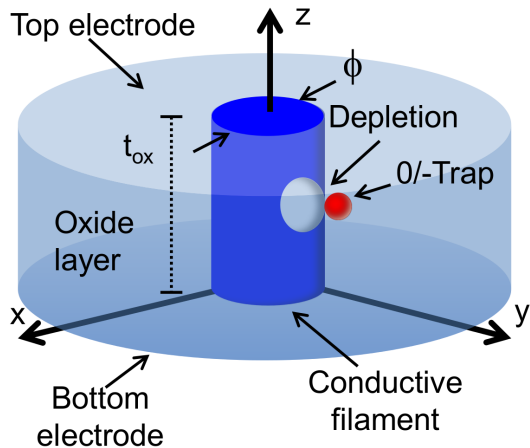
Fig. 2. Schematic picture of the RTN mechanism due to a defect with fluctuating charge at the CF surface. The CF diameter ϕ and the CF height, t_{ox}, equal to the oxide layer thickness, are shown. When the defect is negatively charged, the CF is depleted from carriers within approximately a Debye length. The reduced defect concentration causes the transition to the higher resistance level.

and negative voltage polarities in the low-resistance (set) state. RTN is further evidenced in Fig. 1b, showing the set-state resistance $R = V/I$, obtained from Fig. 1a, and the definition of the resistance change ΔR, namely the difference between the resistance values in correspondence of the two RTN levels. The change of resistance in Fig. 1 can be understood by similar RTN effects taking place in planar MOSFET [11], [12], nanowire MOSFET [13] and Flash memories [14], where RTN arises from a fluctuating charge state of a single trap in the gate dielectric. If negative, the charge depletes part of the inverted channel, thus causing a change to a higher resistance. Similarly, a trap with variable charge state close to the CF can affect the carrier distribution and cause a resistance change in the RRAM, as schematically shown in Fig. 2. In the negative trap state, the CF is depleted from free electrons approximately within a Debye length λ_D [2] given by:

$$\lambda_D = \sqrt{\frac{\epsilon k T}{q^2 n}}, \tag{1}$$

where ϵ is the CF permittivity, k is the Boltzmann constant, T is the temperature, n is the carrier density in the CF and q is the electron charge. The Debye length describes the screening length of the free-electron gas within the CF, controlling the range of Coulombic interaction. As the trap switches to the neutral state, a uniform carrier population is recovered in the CF, resulting in a resistance decrease. Note that positive/neutral states of the defect can similarly explain RTN fluctuations, where a positive defect induces local accumulation (instead of depletion) of electrons within the CF, thus enhancing the conductivity with respect to the neutral state.

III. SIZE-DEPENDENT RTN

Fig. 3a shows the measured resistance as a function of time for variable resistance, obtained by changing I_C during the set
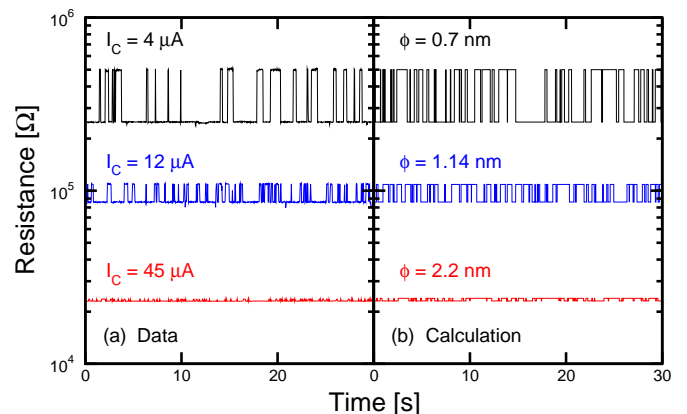

Fig. 3. Measured (a) and calculated (b) resistance as a function of time for variable size of the CF. RTN shows a dependence on CF size, where the relative amplitude $\Delta R/R$ increases at increasing R, thus decreasing CF size.
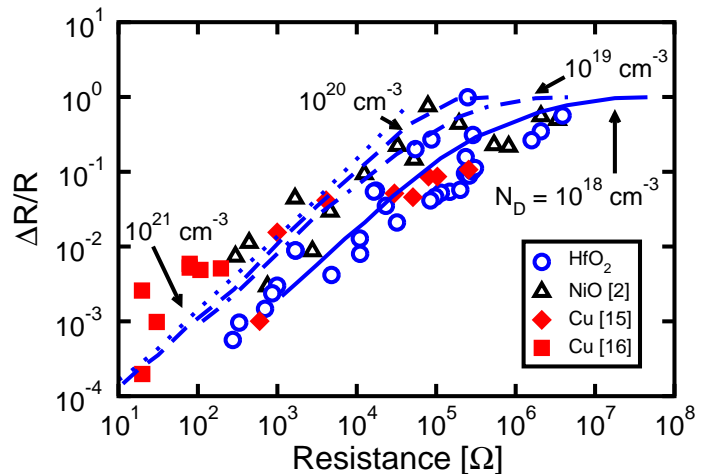

Fig. 4. Measured and calculated $\Delta R/R$ as a function of R. Data for NiO-based RRAM [2], Cu-based electrochemical RRAM [15] and Cu nanobridges [16] are also shown for comparison with HfO$_x$-RRAM data. All data display an universal dependence on R, which can be understood by size-dependent depletion. Calculations were carried out at variable N_D.

transition. About 20 samples were measured for increasing I_C. RTN appeared occasionally after set transition with stochastic change of the amplitude after each set/reset cycle. RTN for reset states with $R > 5 \times 10^5$ Ω showed similar behavior with saturation at $\Delta R/R \approx 0.5$ (not reported in the figure). The resistance change ΔR increases with the resistance levels, as shown by the measured relative resistance change $\Delta R/R$ as a function of the average resistance R in Fig. 4. The figure also reports data from NiO RRAM [2], Cu-based conductive-bridge RAM [15] and Cu nanobridges [16]. All data display an increase of $\Delta R/R$ with R below about 100 kΩ, with a saturation at higher R. The RTN dependence on R was previously explained by the size-dependent carrier depletion within the CF [2]. For small R, corresponding to a large CF where the CF diameter ϕ is much larger than λ_D, the trap-induced depletion impacts only partially on the carrier concentration. As ϕ decreases, the depleted portion of the CF region increases, resulting in an increasing $\Delta R/R$. For
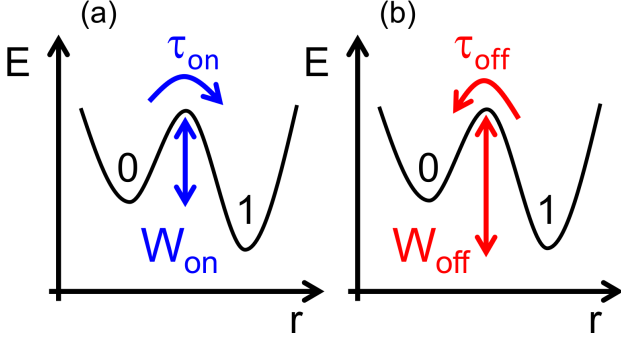
Fig. 5. Energy as a function of a generalized coordinate for the bistable RTN defect, describing transition from low to high resistance (a) and vice versa (b). The transition from low to high resistance requires thermal excitation over a barrier W_{on} in an average time τ_{on}, while the transition from high to low resistance requires excitation over a barrier W_{off} in an average time τ_{off}.

Fig. 6. Map of calculated carrier density for $N_D = 10^{18}$ cm^{-3} and $\phi = 10$ nm (a), for $N_D = 10^{20}$ cm^{-3} and $\phi = 10$ nm (b), for $N_D = 10^{20}$ cm^{-3} and $\phi = 1$ nm (c), and their corresponding cross-section map of electrostatic potential (d, e, f). The applied read voltage was $V_{read} = 50$ mV. Calculations were carried out assuming a negatively charged defect at the CF surface in correspondence of $t_{ox}/2$. The negative defect causes depletion of carrier concentration (a, b, c) and a local potential decrease (d, e, f). Depletion can be partial or full depending on the CF size.

$\phi < \lambda_D$, full depletion occurs, accounting for the saturated $\Delta R/R$ at increasing R. The slope of $\Delta R/R$ in Fig. 4 at low R is approximately 1 in the bi-logarithmic plot, indicating a linear dependence on resistance. This is because R is inversely proportional to the CF area A_{CF}, thus $\left| \frac{\Delta R}{R} \right| \approx \left| \frac{\Delta A_{CF}}{A_{CF}} \right| \propto R$ where $\Delta A_{CF} \approx \lambda_D^2$ is the depleted area [2].

IV. NUMERICAL MODEL OF RTN

To quantitatively account for the size-dependence of $\Delta R/R$ in Figs. 3 and 4, we developed a numerical model for RTN, where we implemented both semiconductor transport equations and switching kinetics through the finite-element method (FEM) using COMSOL®.

A. Transport model

In the model, the CF is described as an n-doped semiconductor nanowire surrounded by an oxide layer as shown in Fig. 2. The RTN trap is modeled as a fixed point charge located in the dielectric. The current density $\vec{J}$ is obtained by the drift-diffusion equation:

$$\vec{J} = qn\mu_n\vec{F} + kT\mu_n\vec{\nabla}n, \qquad (2)$$

where n is the electron density, μ_n is the electron mobility and $\vec{F}$ is the electric field [17]. All calculations were performed under steady-state conditions, thus current continuity reads:

$$\vec{\nabla} \cdot \vec{J} = 0. \qquad (3)$$

The electrostatic potential φ was obtained by solving the Poisson equation:

$$\vec{\nabla} \cdot (-\epsilon\vec{\nabla}\varphi) = q[N_D - n + \chi(x,y,z)], \qquad (4)$$

where N_D is the concentration of dopant atoms, assumed totally ionized, and $\chi(x, y, z)$ describes the fixed charge. In addition, the electric field $\vec{F}$ was linked to the electrostatic potential φ through the equation:
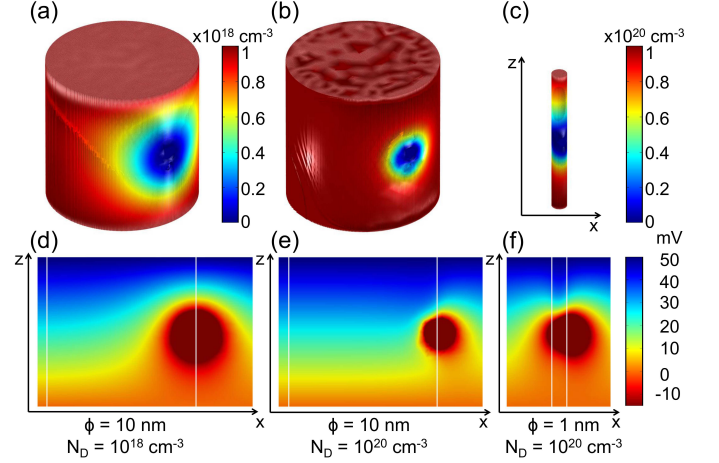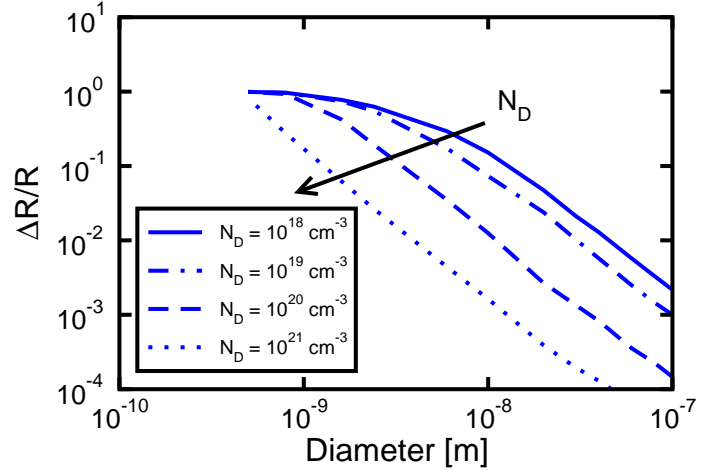
$$\vec{F} = -\vec{\nabla}\varphi. \qquad (5)$$

Fig. 7. Calculated $\Delta R/R$, same simulation results as in Fig. 4, as a function of CF diameter ϕ, evaluated at different doping densities N_D.

The Joule-heating effect due to the flowing current was taken into account by solving the steady-state Fourier equation:

$$\vec{\nabla} \cdot (k_{th}\vec{\nabla}T) + \frac{J^2}{qn\mu_n} = 0, \qquad (6)$$

where k_{th} is the thermal conductivity. It is equal to 16 Wm^{-1}K^{-1} in the CF, which is close to the bulk Hafnium thermal conductivity (23 Wm^{-1}K^{-1} [18]), while it is 0.68 Wm^{-1}K^{-1} in the oxide layer [19]. Self-consistent solution of Eqs. (2)-(6) in 3D allows to evaluate the electrostatic potential, the carrier density, the temperature and the total current for variable charge state of the RTN trap, e.g., neutral and negative. From these results, the resistance change ΔR can be estimated for variable CF size and doping.
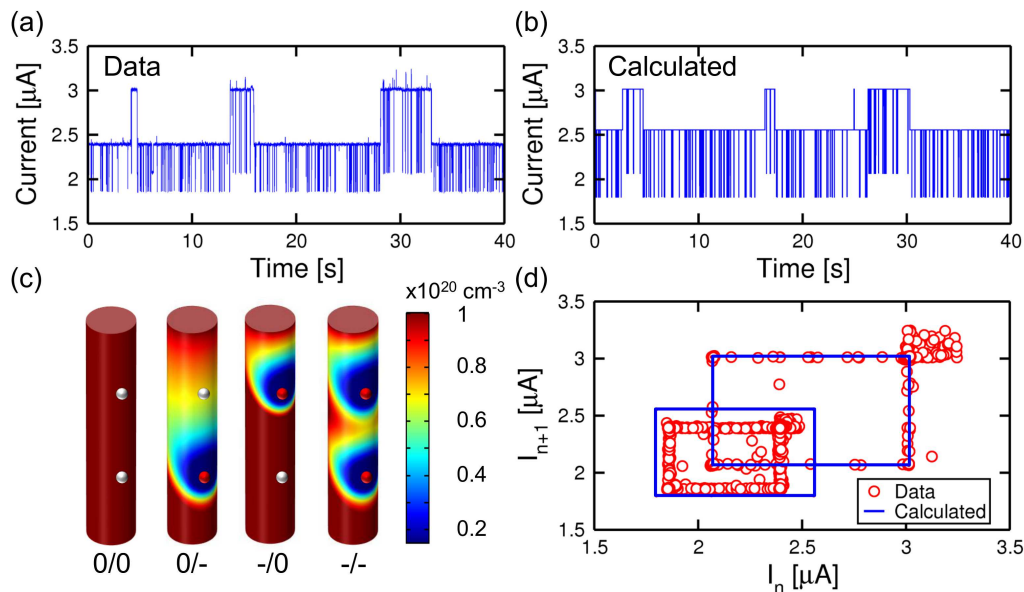
Fig. 8. Measured (a) and calculated (b) current as a function of time featuring complex RTN, the map of calculated carrier density for the four state configurations (c), and the correlation plot of I_{n+1} as a function of I_n (d), where I_n and I_{n+1} are the currents at time t_n and t_{n+1}, respectively.

B. Kinetic model

Fig. 5 shows the defect energy as a function of a generalized coordinate describing the defect configuration. To pass from state 0 to state 1, the trap must overcome a barrier W_{on} (Fig. 5a), which requires an average time τ_{on} given by:

$$\tau_{on} = \tau_0 e^{\frac{W_{on}}{kT}}, \qquad (7)$$

where τ_0 is the pre-exponential factor. Similarly, the reverse transition from 1 to 0 is achieved by overcoming a barrier W_{off} (Fig. 5b), in a corresponding time constant τ_{off} given by:

$$\tau_{off} = \tau_0 e^{\frac{W_{off}}{kT}}. \qquad (8)$$

Generally, the two barriers W_{on} and W_{off} are different, thus resulting in different time constants. The random switching from high to low resistance and viceversa was modeled by a Monte Carlo approach. For every time instant, equal to t_{sample}, a random number is extracted from a uniform distribution between 0 and 1. In the case the number is superior to t_{sample}/τ_{on} and the current is high, the transition to the low current state happens. The same procedure is employed in the low current state, switching to the high current state if the extracted value is above t_{sample}/τ_{off}.

C. Simulation results

Fig. 3b shows the calculated RTN characteristics for different CF diameters ϕ and Fig. 4 reports the calculated ΔR obtained with the model for variable N_D. The doping concentration reflects the local concentration of defects, such as oxygen vacancies, typically acting as n-type dopants in transition metal oxides [20], [21]. The resistance change is shown to depend on both doping and CF size, hence resistance. The simulation results in Fig. 4 closely account for the observed $\Delta R/R$ in different material systems.

Fig. 6 provides a closer look at the simulations, showing the calculated carrier density n (a), (b), (c) and electrostatic potential φ (d), (e), (f) in the CF for an applied voltage $V_{read} = 50$ mV. In the calculations, a negative charge $-q$ was assumed in the RTN trap on the surface of the CF with diameter $\phi = 10$ nm, length $L = 10$ nm and doping concentration $N_D = 10^{18} \mathrm{cm}^{-3}$ (a), resulting in a resistance $R = 130$ kΩ. The trap induces a local lowering of the electrostatic potential (d), causing a local depletion according to Eq. (2). The radius of the depletion region is approximately 3 nm, close to the Debye length $\lambda_D = 5$ nm according to Eq. (1), assuming $\epsilon_r = 15.6$ [22] and $N_D = 10^{18}$ cm^{-3}. Since λ_D is smaller than ϕ, partial depletion takes place, thus causing $\Delta R/R \approx 0.15$ in the linear regime of Fig. 4. Note that the total image charge induced by the defect within the CF is of the order of $+q$. This is comparable to the total number of electrons in the CF, which can be evaluated as $N_D L \pi \phi^2 \approx 3.1$ electrons in Fig. 6a. This highlights the relevance of single-charged defect fluctuations for RRAM current noise.

Fig. 6 also shows the calculated n (b) for the same CF properties of Fig. 6a, except for a doping concentration $N_D = 10^{20}$ cm^{-3}. The resulting resistance was $R = 1.2$ kΩ. Due to the increased doping, the depleted region (see Fig. 6e) reduces to about $\lambda_D = 0.5$ nm, thus causing a resistance change $\Delta R/R \approx 0.02$, thus significantly smaller than the relative resistance change in Fig. 6a. To study the size dependence of RTN, Fig. 6 shows the calculated n (c) and φ (f) for a smaller diameter $\phi = 1$ nm, assuming a doping concentration $N_D = 10^{20}$ cm^{-3}. As the CF diameter becomes comparable to λ_D, carriers are fully depleted in the whole CF cross section, resulting in a large resistance change $\Delta R/R \approx 0.8$. The regimes of partial depletion (Figs. 6a and 6b) and full depletion (Fig. 6c) account for the linear and saturated R-dependence of RTN in Fig. 4 respectively. Note that, for the same N_D, the CF size also affects the potential profile within the dielectric,
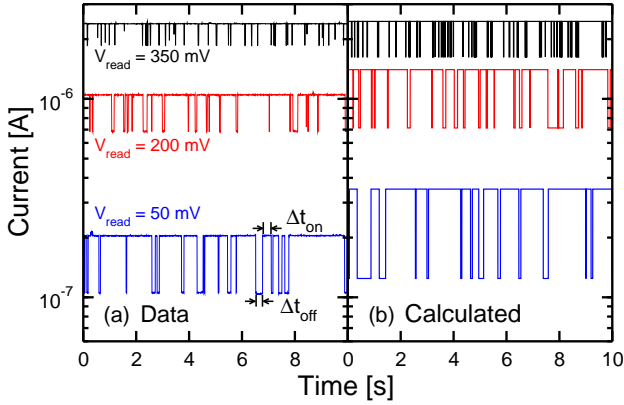
Fig. 9. Measured current as a function of time for read voltage V_{read} = 50, 200 and 350 mV (a) and corresponding calculations (b). The RTN switching times, namely Δt_{on} and Δt_{off} shown in the figure, decrease with V_{read}.
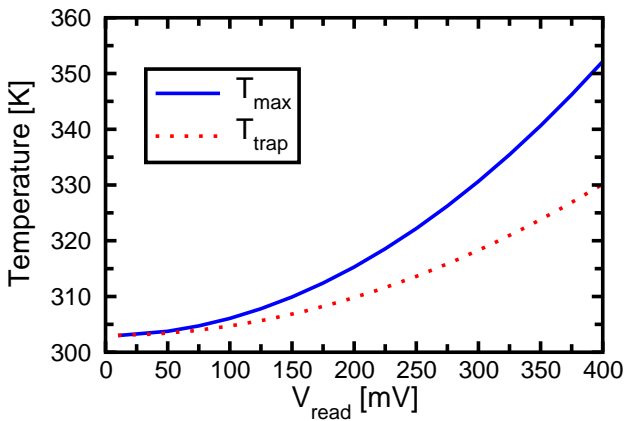

Fig. 10. Calculated temperature as a function of the applied V_{read} in the center of the CF T_{max}, solid line, and in proximity of the trap T_{trap}, dashed line.

as a result of the dipole of the negative trap charge and of the positive image charge induced in the CF. Note that, for any given CF size, the change of resistance increases at decreasing N_D. This is demonstrated in Fig. 7, reporting the calculations of Fig. 4 as a function of the CF diameter ϕ. For a given CF size, e.g., 5 nm, the relative change of resistance $\Delta R/R$ decreases with N_D due to the increased screening within the CF.

V. COMPLEX RTN

The kinetic model for trapping/detrapping in Fig. 2 allows to simulate not only two-level RTN, as in Fig. 3, but also complex RTN due to multiple defects. Fig. 8a shows the measured current as a function of time displaying four discrete levels, which can be understood by two independent defects both affecting the carrier concentration in the CF [23]. Fig. 8b shows the calculated current as a function of time, while Fig. 8c shows the map of calculated carrier concentration within the CF. Here, the two traps can display two charged states, namely neutral (0) or negative (-), thus resulting in four CF states, namely 0/0, corresponding to the highest current level, 0/-, -/0 and -/-, corresponding to the lowest current
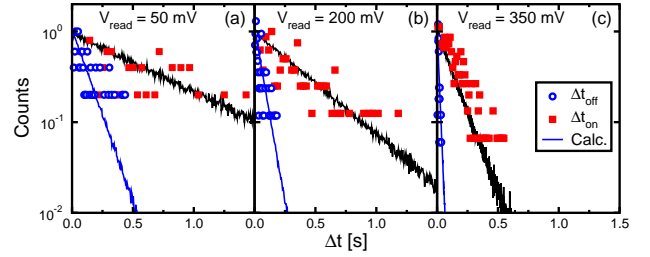

Fig. 11. Distributions of Δt_{on} and Δt_{off} for increasing read voltage, namely V_{read} = 50 mV (a), 200 mV (b) and 350 mV (c). The distributions of both measured and calculated times are shown, showing an exponential shape which is consistent with the random switching in RTN. The average values of the distribution correspond to the average transition times τ_{on} and τ_{off} in Fig. 5.

level. The activation energies were properly chosen to yield a relatively fast trap and a relatively slow trap as apparent from the RTN switching characteristics.

Fig. 8d shows the correlation plot of read current I_{n+1} at time t_{n+1} as a function of the current I_n measured at the previous read time t_n [9], [23]. The two squares appearing in the correlation plot represent the two independent fluctuators [23], while the additional scattered points at the top/right corners of the squares result from background 1/f noise. The two squares have different size, since the RTN amplitude of one trap depends on the state of the other trap, e.g., the change of the current from 0/0 to 0/- is larger than the change of the current from -/0 to -/-. This is due to the partial overlap between the depletion regions of the two defects in the negatively-charged state, as shown in Fig. 8c. Note that data points can be found along the sides of the square in Fig. 8d, which is due to the integration time in our current measurements being comparable to τ_{on} and τ_{off}. As the current switches from one level to the other during integration, the resulting value of the current is intermediate between the extreme values in the RTN. As a result, the corresponding point in the scatter plot falls on one of the four sides of the square in Fig. 8d. Complex RTN was found with relatively low probability in our samples, since it requires two fluctuating defects near the same CF. For this reason, it might be expected that complex RTN can be seen more easily in states at relatively low R, due to the relatively large surface of the CF.

VI. BIAS DEPENDENCE OF RTN SWITCHING RATES

Data in Fig. 1 show that RTN transition rate increases with the read voltage V_{read}, while ΔR decreases for increasing V_{read}. To understand the voltage dependence of RTN, Fig. 9a shows the measured read current as a function of time at room temperature ($T_0 = 30$ °C) for increasing voltage, namely V_{read} = 50 mV, 200 mV and 350 mV. The three measurements were done at three different initial times and are referred to the same time interval only for the purpose of comparison. The switching rates between the high and low current states clearly increase with V_{read}. To better characterize the switching times, we defined Δt_{on} as the time for which the current remains high, and Δt_{off} as the time for which the current remains low
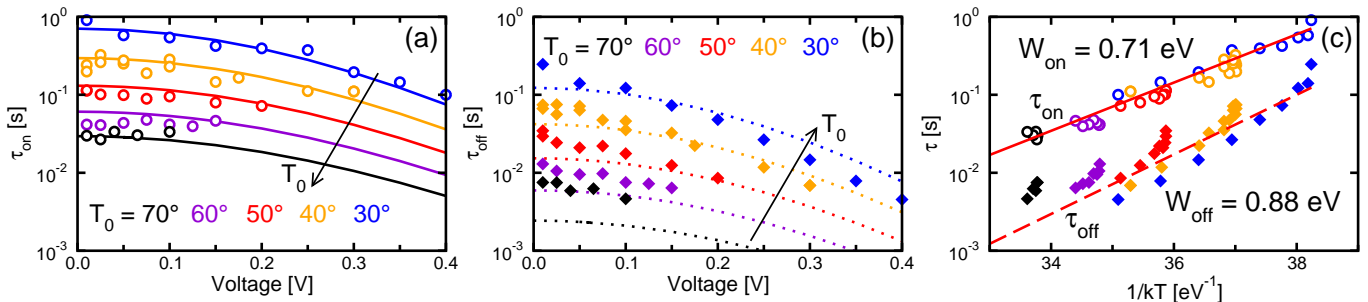
Fig. 12. Measured and calculated τ_{on} (a) and τ_{off} (b) as a function of read bias for increasing ambient temperature T_0 from 30 to 70 °C, and Arrhenius plot of the experimental and calculated τ_{on} and τ_{off} as a function of $1/kT$, where the local temperature at the RTN defect was calculated by the numerical model. The straight lines indicate Arrhenius behavior with energy barriers W_{on} = 0.71 eV and W_{off} = 0.88 eV.

(see examples in Fig. 9a). Both Δt_{on} and Δt_{off} decrease for increasing V_{read}. Fig. 11 shows the probability distributions of measured Δt_{on} and Δt_{off} for V_{read} = 50 mV, 200 mV and 350 mV. The distributions display an exponential shape, consistent with the random switching model in Fig. 5, where the time constants τ_{on} and τ_{off} correspond to the average values in the distributions of Fig. 5. The distributions clearly show an acceleration of RTN switching for increasing V_{read}.

The RTN was calculated with our model at variable V_{read} to study the voltage dependent RTN. Fig. 9b shows the calculated current as a function of time at increasing V_{read} = 50, 200 and 350 mV. Fig. 11 shows the calculated Δt_{on} and Δt_{off} for V_{read} = 50 mV, 200 mV and 350 mV. In both cases, the model accurately captures the V_{read} dependence. In the model, the acceleration of RTN switching kinetics is due to Joule heating induced by the read voltage and current according to the Fourier equation in Eq. (6). For increasing V_{read}, Joule heating enhances the temperature at the defect site as shown in Fig. 10, thus accelerating the transition time according to the Arrhenius law in Eqs. (7) and (8). Note that migration might lead to voltage-dependent changes of resistance due to a change of shape of the CF. However, these changes are expected to be monotonic, or multistable, since migration involves the transfer of defects in one direction only, as opposed to the bistable fluctuation of RTN.

To further confirm the Joule heating model for voltage-dependent RTN, experiments were conducted at variable V_{read}, between 0 V and 0.4 V, and variable room temperature T_0, between 30 and 70 °C. Fig. 12 shows the measured and calculated results for τ_{on} (a) and τ_{off} (b), namely the average switching times for RTN, as a function of V_{read} for increasing T_0. For any given T_0, both time constants decrease for increasing V_{read}, in agreement with results in Figs. 9 and 11. On the other hand, for any given V_{read}, the time constants decrease with T_0. Both dependences can be understood by the impact of Joule heating on the transition kinetics of Eqs. (7) and (8), where the switching times decrease with the local temperature T, which is enhanced by both the ambient temperature T_0 and by V_{read}. Fig. 12c shows the Arrhenius plot of τ_{on} and τ_{off} taken from Figs. 12a and b. In this plot, T was calculated from the numerical model assuming a CF with diameter ϕ = 0.77 nm and a defect located at a distance of 0.5 nm from the CF surface and at a distance of 2.5
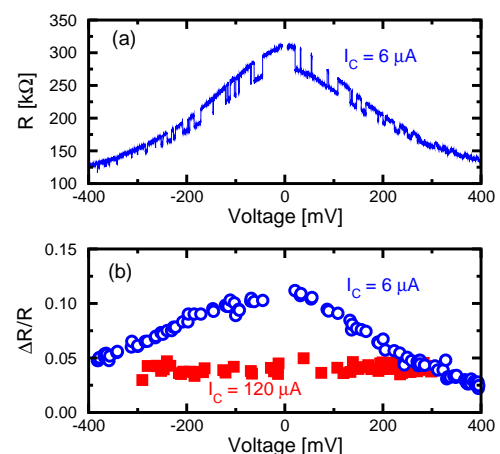

Fig. 13. Measured R for I_C = 6 μA (a) and $\Delta R/R$ for I_C = 6 μA and I_C = 120 μA (b) as a function of V_{read}. The decrease of R and of $\Delta R/R$ with V_{read} for I_C = 6 μA is consistent with PF conduction and its response to a fluctuating charge as shown in Fig. 14. The relative resistance change $\Delta R/R$ remains constant for I_C = 120 μA due to metallic transport in large CFs.

nm from the top electrode. Data display a universal Arrhenius dependence with energy barriers W_{on} = 0.71 eV and W_{off} = 0.88 eV for τ_{on} and τ_{off}, respectively. These energy barriers should not be viewed as characteristic values for HfO_x, since other defects with smaller/larger barriers may be expected. In fact, significantly larger/smaller RTN times than the 0.1-1 s time range considered in our work may be possible for RTN switching.

VII. BIAS DEPENDENCE OF ΔR

Fig. 1b also shows that the resistance change ΔR decreases for increasing V_{read}. This is particularly evident for relatively small I_C, as shown by the measured R as a function of V_{read} for I_C = 6 μA in Fig. 13a. Note the symmetric and non-linear behavior of R, which is consistent with PF transport in the CF. Also, the switching rates display the same dependence for positive and negative V_{read}, since T only depends on the absolute value of V_{read}. Fig. 13b shows the corresponding $\Delta R/R$ for I_C = 6 μA (from Fig. 13a) and I_C = 120 μA. Data at I_C = 6 μA clearly show a decrease of $\Delta R/R$ with V_{read}, while $\Delta R/R$ negligibly depends on V_{read} for I_C = 120 μA.
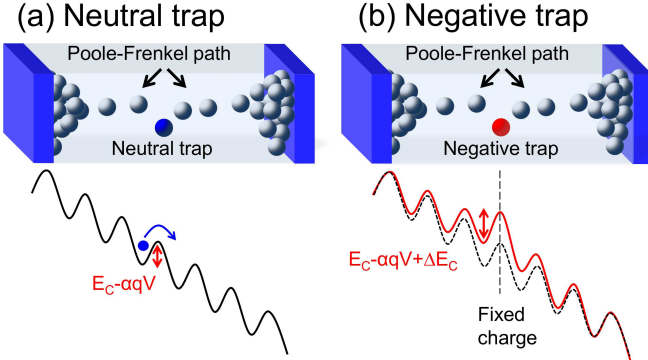
Fig. 14. Schematic illustration of the PF transport in a few-defect CF. For a neutral defect, R is controlled by an energy barrier E_C (b), while the transition to a negative charge causes an increase of energy barrier by ΔE_C.

Fig. 15. Arrhenius plot of $1 + \Delta R/R$ for $I_C = 6$ μA and $I_C = 120$ μA, for both positive and negative V_{read}. The defect temperature was estimated from Eq. (12). The straight line for $I_C = 6$ μA is in agreement with the PF model of Eq. (11), while the constant $\Delta R/R$ for $I_C = 120$ μA can be explained by metallic conduction in the CF.

This behavior can be understood by the different conduction regimes taking place in small and large CFs. A small CF can consist of only few defects, acting as localized states for PF hopping of electrons, while a large CF contains many more defects resulting in a doped-semiconductor behavior or even a metallic-like conduction for extremely large defect concentration, e.g., $N_D = 10^{21}$ cm^{-3}. Fig. 14 schematically shows the PF conduction picture and the impact of a RTN switching defect close to the CF. When the RTN defect is in the neutral state (Fig. 14a), electrons migrate in response to the applied voltage V_{read}, and the CF resistance can be written as:

$$R = R_0 e^{\frac{E_C - \alpha q V}{kT}}, \tag{9}$$

where R_0 is a pre-exponential factor, α is the barrier lowering coefficient and E_C is the characteristic energy barrier for electron hopping. For a negatively-charged defect (Fig. 14b), the defect potential influences the electrostatic potential in the CF, thus enhancing the hopping barrier by an additional contribution ΔE_C. Therefore, the resistance increases according to:

$$R = R_0 e^{\frac{E_C + \Delta E_C - \alpha q V}{kT}}. \tag{10}$$

From Eqs. (9) and (10), the ratio $\Delta R/R$ reads:

$$\frac{\Delta R}{R} = \frac{R' - R}{R} = e^{\frac{\Delta E_C}{kT}} - 1, \tag{11}$$

where an increase of T, due to a larger V_{read}, leads to a decrease of $\Delta R/R$. Fig. 15 shows the $1 + \Delta R/R$ from Fig. 14b for both $I_C = 6$ μA and $I_C = 120$ μA. In the calculations, the temperature was simply evaluated by:

$$T = T_0 + \frac{R_{th}}{R} V^2, \tag{12}$$

which is the analytical solution of Eq. (6) for a cylindrical CF with resistance R and an effective thermal resistance $R_{th} = t_{ox}/(8 k_{th} A_{CF})^2$ [24], where an effective thermal conductivity $k_{th} = 16$ Wm^{-1}K^{-1} was assumed to describe heating at the RTN defect site. Data at small I_C in Fig. 15 display an Arrhenius behavior with slope $\Delta E_C = 4.1$ meV
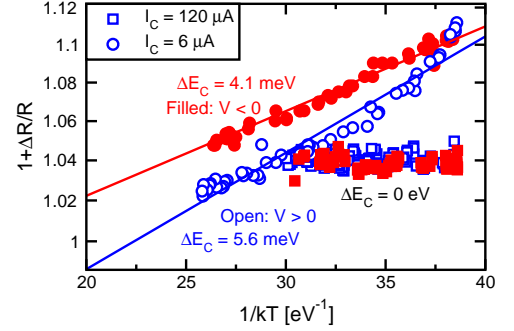
for $V_{read} < 0$ and 5.6 meV for $V_{read} > 0$, which is consistent with Eq. (11). The polarity-dependent ΔE_C might be due to different position of the energy maximum between two localized states with respect to the RTN defect for positive and negative V_{read}. For $I_C = 120$ μA, $\Delta R/R$ is almost constant, which can be explained by conduction being due to doped-semiconductor or metallic transport. For PF-type CFs achieved at low I_C, the immunity to RTN increases for increasing V_{read}. This is due to the increased switching rate, which allows for a better averaging between the two resistance levels, and to the reduced RTN amplitude. Therefore, reading at relatively large V_{read} may considerably reduce read error in RRAM. However, a practical limit for the increase of V_{read} is given by read disturb, where the high read voltage may induce migration because of excessive heating and field. The optimum read voltage thus arises from a careful tradeoff between RTN reduction and read disturb.

VIII. CONCLUSIONS

RTN in RRAM devices is studied through a 3D numerical model, where the random fluctuation between two levels is explained by the change of charge state in a bistable defect close to the CF. The model provides a physical quantitative description of both the electron transport in presence of a fluctuating defect and the temperature-dependent switching kinetics. The model accounts for the size dependence of RTN amplitude, which is due to the partial or full depletion of carriers depending on the CF diameter, and for bias dependence of RTN switching. The average switching times are shown to decrease with voltage, which is explained by Joule heating induced by V_{read}. The relative change of resistance also decreases with V_{read} for relatively large R, which is due to the impact of the negatively-charged defect potential on the energy barrier for PF conduction. In support of this interpretation, metallic CFs are shown to display no V_{read}-dependence of the relative resistance change. These results suggest that increasing V_{read} may significantly reduce the impact of RTN on read errors.

IX. ACKNOWLEDGMENTS

REFERENCES

[1] S. Ambrogio, S. Balatti, A. Cubeta, A. Calderoni, N. Ramaswamy, and D. Ielmini, "Statistical fluctuations in HfO_x resistive-switching memory (RRAM): Part I - Set/Reset variability," *IEEE Trans. Electron Devices*, vol. submitted, 2014.

[2] D. Ielmini, F. Nardi, and C. Cagli, "Resistance-dependent amplitude of random telegraph-signal noise in resistive switching memories," *Appl. Phys. Lett.*, vol. 96, no. 5, p. 053503, 2010.

[3] S. Yu, X. Guan, and H.-S. P. Wong, "On the stochastic nature of resistive switching in metal oxide RRAM: Physical modeling, monte carlo simulation, and experimental characterization," *IEDM Tech. Dig.*, pp. 275–278, 2011.

[4] Z. Fang, H. Y. Yu, W. J. Fan, G. Ghibaudo, J. Buckley, B. DeSalvo, X. Li, X. P. Wang, G. Q. Lo, and D. L. Kwong, "Current conduction model for oxide-based resistive random access memory verified by low.frequency noise analysis," *IEEE Trans. Electron Devices*, vol. 60, no. 3, pp. 1272–1275, 2013.

[5] D. Veksler, G. Bersuker, L. Vandelli, A. Padovani, L. Larcher, A. Muraviev, B. Chakrabarti, E. Vogel, D. C. Gilmer, and P. D. Kirsch, "Random telegraph noise (RTN) in scaled RRAM devices," *International Reliability Physics Symposium (IRPS)*, pp. 101–104, 2013.

[6] N. Raghavan, R. Degraeve, A. Fantini, L. Goux, S. Strangio, B. Govoreanu, D. J. Wouters, G. Groeseneken, and M. Jurczak, "Microscopic origin of random telegraph noise fluctuations in aggressively scaled RRAM and its impact on read disturb variability," *International Reliability Physics Symposium (IRPS)*, pp. 5E.3.1–5E.3.7, 2013.

[7] F. T. Chen, H.-Y. Lee, Y.-S. Chen, S. Z. Rahaman, C.-H. Tsai, K.-H. Tsai, T.-Y. Wu, W.-S. Chen, P.-Y. Gu, Y.-D. Lin, S.-S. Sheu, M.-J. Tsai, L.-H. Lee, T.-K. Ku, and P.-S. Chen, "Resistance instabilities in a filament-based resistive memory," *International Reliability Physics Symposium (IRPS)*, pp. 5E.1.1–5E.1.7, 2013.

[8] K. Prall, N. Ramaswamy, W. Kinney, K. Holtzclaw, X. Che, J. Strand, and R. Bez, "An update on emerging memory: Progress to 2Xnm," *International Memory Workshop IMW*, pp. 1–5, 2012.

[9] F. M. Puglisi, P. Pavan, A. Padovani, L. Larcher, and G. Bersuker, "RTS noise characterization of HfO_x RRAM in high resistive state," *Solid State Electronics*, vol. 84, pp. 160–166, 2013.

[10] S. Ambrogio, S. Balatti, A. Cubeta, A. Calderoni, N. Ramaswamy, and D. Ielmini, "Understanding switching variability and random telegraph noise in resistive RAM," *IEDM Tech. Dig.*, pp. 782–785, 2013.

[11] K. S. Ralls, W. J. Skocpol, L. D. Jackel, R. E. Howard, L. A. Fetter, and R. W. E. et al., "Discrete resistance switching in submicrometer silicon inversion layers: individual interface traps and low-frequency (1/f?) noise," *Phys. Rev. Lett.*, vol. 52, no. 3, pp. 228–231, 1984.

[12] K. K. Hung, P. K. Ko, C. Hu, and Y. C. Cheng, "Random telegraph noise of deep-submicrometer MOSFETs," *IEEE Electron Device Lett.*, vol. 11, no. 2, pp. 90–92, 1990.

[13] A. N. Nazarov, I. Ferain, N. D. Akhavan, P. Razavi, R. Yu, and J. P. Colinge, "Random telegraph-signal noise in junctionless transistors," *Appl. Phys. Lett.*, vol. 98, p. 092111, 2011.

[14] A. Ghetti, C. Compagnoni, A. Spinelli, and A. Visconti, "Comprehensive analysis of random telegraph noise instability and its scaling in deca-nanometer flash memories," *IEEE Trans. Electron Devices*, vol. 56, no. 8, pp. 1746–1752, 2009.

[15] R. Soni, P. Meuffels, A. Petraru, M. Weides, C. Kugeler, R. Waser, and H. Kohlstedt, "Probing Cu doped $Ge_{0.3}Se_{0.7}$ based resistance switching memory devices with random telegraph noise," *J. Appl. Phys.*, vol. 107, no. 2, p. 024517, 2010.

[16] K. S. Ralls and R. A. Buhrman, "Microscopic study of 1/f noise in metal nanobridges," *Phys. Rev. B*, vol. 44, p. 5800, 1991.

[17] R. F. Pierret, "Semiconductor device fundamentals," *Addison Wesley*, vol. 2nd ed., 1996.

[18] D. R. L. (ed), "CRC handbook of chemistry and physics, 84th edition," *CRC Press. Boca Raton, Florida*, 2003.

[19] M. A. Panzer, M. Shandalov, J. A. Rowlette, Y. Oshima, Y. W. Chen, P. C. McIntyre, and K. E. Goodson, "Thermal properties of ultrathin hafnium oxide gate dielectric films," *IEEE Electron Device Lett.*, vol. 30, no. 12, pp. 1269–1271, 2009.

[20] G. W. Tomlins, J. L. Routbort, and T. O. Mason, "Zinc self-diffusion, electrical properties, and defect structure of undoped, single crystal zinc oxide," *J. Appl. Phys.*, vol. 87, no. 1, pp. 117–123, 2000.

[21] J. Nowotny, M. Radecka, and M. Rekas, "Semiconducting properties of undoped TiO_2," *J. Phys. Chem. Solids*, vol. 58, no. 6, pp. 927–937, 1997.

[22] A. Callegari, E. Cartier, M. Gribelyuk, H. F. Okorn-Schmidt, and T. Zabel, "Physical and electrical characterization of hafnium oxide and hafnium silicate sputtered films," *J. Appl. Phys.*, vol. 90, pp. 6466–6475, 2001.

[23] T. Nagumo, K. Takeuchi, S. Yokogawa, K. Imai, and Y. Hayashi, "New analysis methods for comprehensive understanding of random telegraph noise," *IEDM Tech. Dig.*, pp. 759–762, 2009.

[24] D. Ielmini, "Modeling the universal set/reset characteristics of bipolar RRAM by field- and temperature-driven filament growth," *IEEE Trans. Electron Devices*, vol. 58, no. 12, pp. 4309–4317, 2011.